



Deposited via The University of Sheffield.

White Rose Research Online URL for this paper:

<https://eprints.whiterose.ac.uk/id/eprint/222043/>

Version: Accepted Version

---

**Article:**

Panarin, Y.P., Jiang, W., Yadav, N. et al. (2025) Colossal dielectric permittivity and superparaelectricity in phenyl pyrimidine based liquid crystals. *Journal of Materials Chemistry C*, 13 (3). pp. 1507-1518. ISSN: 2050-7526

<https://doi.org/10.1039/d4tc03561e>

---

© 2025 The Authors. Except as otherwise noted, this author-accepted version of a journal article published in *Journal of Materials Chemistry C* is made available via the University of Sheffield Research Publications and Copyright Policy under the terms of the Creative Commons Attribution 4.0 International License (CC-BY 4.0), which permits unrestricted use, distribution and reproduction in any medium, provided the original work is properly cited. To view a copy of this licence, visit <http://creativecommons.org/licenses/by/4.0/>

**Reuse**

This article is distributed under the terms of the Creative Commons Attribution (CC BY) licence. This licence allows you to distribute, remix, tweak, and build upon the work, even commercially, as long as you credit the authors for the original work. More information and the full terms of the licence here:

<https://creativecommons.org/licenses/>

**Takedown**

If you consider content in White Rose Research Online to be in breach of UK law, please notify us by emailing [eprints@whiterose.ac.uk](mailto:eprints@whiterose.ac.uk) including the URL of the record and the reason for the withdrawal request.

# Colossal Dielectric Permittivity and Superparaelectricity in phenyl pyrimidine based liquid crystals

Yuri P. Panarin<sup>1,2#</sup>, Wanhe Jiang<sup>3#</sup>, Neelam Yadav<sup>1#</sup>, Mudit Sahai<sup>1,4</sup>, Yumin Tang<sup>5</sup>, Xiangbing Zeng<sup>5</sup>, O. E. Panarina<sup>1</sup>, Georg H. Mehl<sup>3\*</sup>, Jagdish K. Vij<sup>1\*</sup>

<sup>1</sup>Department of Electronic and Electrical Engineering, Trinity College Dublin, The University of Dublin, Dublin 2, Ireland

<sup>2</sup>Department of Electrical and Electronic Engineering, TU Dublin, Dublin 7, Ireland

<sup>3</sup>Department of Chemistry, University of Hull, Hull HU6 7RX, UK

<sup>4</sup>Department of Physics, Birla Institute of Technology and Science, Pilani, India

<sup>5</sup>Department of Materials Science and Engineering, University of Sheffield, Sheffield, S1 3JD, UK

A set of polar rod-shaped liquid crystalline molecules with dipole moments ( $\mu > 10.4$ - $14.8$  D), and molecular structures based on the ferroelectric nematic prototype DIO, are designed, synthesized, and investigated. When the penultimate fluoro-phenyl ring is replaced by phenylpyrimidine moiety, the molecular dipole moment increases from 9.4 D for DIO to 10.4 D for the new molecule and when the terminal fluoro- group is additionally replaced by the nitrile group, the dipole moment rises to 14.8 D. Such a replacement enhances not only the net dipole moment of the molecule, but it also reduces the steric hindrance to rotations of the moieties within the molecule. The superparaelectric nematic (N) and smectic A (SmA) phases of these compounds are found to exhibit colossal dielectric permittivity, obtained both from dielectric spectroscopy, and capacitance measurements using a simple capacitor divider circuit. The electric polarization is measured vs. the field ( $E$ ). However, almost no hysteresis in  $P$  vs.  $E$  is found in the nematic and smectic A phases. The colossal dielectric permittivity persists over the entire fluidic range. The experimental results lead us to conclude that these materials belong to the class of superparaelectrics (SPE) rather than to ferroelectrics due to the absence of hysteresis and the linear dependence of  $P$  on  $E$ . The synthesized organic materials are the first fluids for which superparaelectricity is discovered and furthermore these show great potential for applications in supercapacitors used for storing energy.

---

# joint first authors

\*Corresponding authors: Y. Panarin: [yuri.panarin@tudublin](mailto:yuri.panarin@tudublin), G. Mehl: [G.H.Mehl@hull.ac.uk](mailto:G.H.Mehl@hull.ac.uk);

J. K. Vij: [jvij@tcd.ie](mailto:jvij@tcd.ie)

**Key words: Ferroelectric nematics, superparaelectric fluids, Colossal dielectric permittivity**

## 42 **1. Introduction**

43 In electronics industries, the need for increasing the device density goes hand in hand  
44 with miniaturization of electronic structures that continue working efficiently with decreasing  
45 size to the nanoscale level. The micro and nano electronic devices thus require replacement of  
46 the conventional dielectric materials with those exhibiting colossal dielectric permittivity (CP).  
47 CP has been observed in solid state ferroelectric and superparaelectric (SPE) perovskite related  
48 materials. The concept of superparaelectricity, introduced recently [1] is somewhat analogous  
49 to superparamagnetism (SPM). The electric polarization induced by the field is identified as  
50 superparaelectric with the basic property of the materials having CP. In an analogous case of  
51 magnetism, the theory of the ordered states based on isolated spins has been worked out. A  
52 superparamagnetic state includes small clusters of ordered spins with adequate magneto-  
53 crystalline anisotropic energy that maintain stability against thermal fluctuations. However,  
54 no theory is yet established for the solid SPE though polar clusters of varying sizes may exist  
55 to form a polar order.

56 These range mainly from the transition metal oxides [2,3] to two-dimensional nanosheet  
57 hybrids, the latter are based on reduced graphene oxide. [4] These systems are found having  
58 varying dependencies of the permittivity on temperature and frequency. For example, some  
59 SPE materials show CP independent of frequency up to the GHz range [5], while others such as  
60 the relaxor ferroelectrics show strong resonance-type frequency dependence of the permittivity  
61 [1]. In the paraelectric state, [1,5] the solid state materials show softening of the permittivity with  
62 temperature increasing (soft mode), and in some cases the permittivity rises with increase in  
63 temperature. Due to these unusual properties for the new phenomenon, the paraelectric state  
64 is described as superparaelectric (SPE). The SPE materials have two common features (i)  
65 Colossal Permittivity CP [6] and (ii) the paraelectric type response (i.e. hysteresis-free linear  
66 P-E response).

67 The first examples of fluids that exhibit colossal dielectric permittivity are the recently  
68 observed ferroelectric nematics,[7, 8, 9,10] characterized by (i) extremely large dipole moments  
69 ( $\mu \sim 10$  D), (ii) colossal dielectric permittivity ( $\epsilon' \sim 10,000$ ) and (iii) the high spontaneous  
70 polarization ( $P_s \sim 5 \mu\text{C}/\text{cm}^2$ ) [11,12]. Such high dielectric permittivity was explained by two  
71 different theoretical models [13,14] and [15,16,17]. Interestingly, some materials show optical  
72 activity from mirror symmetry breaking [18,19,20] in both the ferroelectric and paraelectric  
73 nematic phases. Though several new organic ferroelectric compounds [21,22,23,24,25,26,27,28]  
74 continue being reported and discussed in the literature every week, many critical issues need  
75 addressing prior to fabricating and launching devices for applications. Though the structure

76 property relationship of ferroelectric nematics has not yet been worked out, two major causes  
77 for the emergence of this phase have been found. These are (i) the magnitude of the molecular  
78 dipole moment and (ii) the relative spatial distribution of dipole moments of groups and or the  
79 charge distribution created within the molecule. Finally, the short and the long-range  
80 intermolecular interactions of the dipole moments of molecules lead to the mesoscale  
81 synergistic properties that need investigations.

82 In the quest for finding a novel class of high-dielectric constant organic materials based  
83 on the prototype molecule DIO [7], Table 1, the molecular design includes enhancing its dipole  
84 moment. Large molecular dipole moment is also the pre-requisite for obtaining large dielectric  
85 permittivity. In addition, the short-range Kirkwood Frohlich correlation parameter of the  
86 dipole moments <sup>[29]</sup> also plays an important role. In this paper, new molecules based on the  
87 substituted phenylpyrimidine motif are designed, synthesized, and investigated. Polarizing  
88 optical microscopy, X-ray scattering, electrical studies, and dielectric spectroscopy are used to  
89 characterize different phases of two new compounds. Large values of the dielectric  
90 permittivity imply dipolar orientation of the polar clusters at a microscopic level in the medium.  
91 Evidence for the existence of super paraelectricity in these materials is presented in terms of  
92 the absence of saturated polarization as a proof.

93

## 94 **2. Experimental Section**

### 95 **2.1. Sample preparation for dielectric, optical and electro-optical studies.**

96 For achieving planar alignment where required, Indium tin oxide (ITO) coated glass substrates  
97 are spin coated with RN 1175 (Nissan chemicals, Japan) and polymerized at a temperature of  
98 250 °C for 1 hour. The coated surfaces are subsequently rubbed with a rotating commercial  
99 rubbing machine. While the homeotropic cells are coated with AL60702 (JSR Korea) and  
100 polymerized at 80 °C for 15 minutes and at 110 °C for 15 minutes respectively. Commercial  
101 cells procured from E.H.C ltd., Japan are also used for some of the measurements. The cell  
102 thickness was controlled by Mylar spacers of different thicknesses and it was measured by  
103 optical interference technique. LC cells of these samples are studied using polarizing optical  
104 microscope (Olympus BX 52) equipped with an INSTEC's hot stage. The temperature is  
105 controlled by Eurotherm 2604 and system designed to obtain temperature stabilization within  
106  $\pm 0.02^\circ\text{C}$

### 107 **2.2. Differential Scanning Calorimetry**

108 The DSC is investigated using Perkin Elmer Differential Scanning Calorimeter DSC 4000,  
109 using aluminum pans and calibrated against indium standard. DSC results are expressed in

110 terms of the onset temperatures for second heating and the cooling curve. The heating rate, if  
111 not stated is 10 °C/min.

### 112 **2.3. Birefringence Measurements**

113 The birefringence measurements are made using an optical spectral technique [30] on a planar  
114 homogenous aligned 25 μm thick cell. The transmittance (T) spectrum of the cell from  
115 achromatic light source is measured using Avantes AvaSpec-2048 fiber spectrometer as a  
116 function of temperature. The transmittance T of a homogeneous planar aligned cell is given  
117 by:

$$118 \quad T = A \sin^2 \left( \frac{\pi \cdot \Delta n(\lambda) \cdot d}{\lambda} \right) + B \quad (9)$$

119 where  $A$  is the amplitude factor,  $B$  is leakage offset,  $d$  is the cell thickness and  $\Delta n(\lambda) = k \cdot$   
120  $\frac{\lambda^2 \cdot \lambda^{*2}}{\lambda^2 - \lambda^{*2}}$  is the birefringence dispersion governed by the extended Cauchy equation.

121 Here  $k$  is a temperature-dependent scaling factor proportional to the order parameter (S). In  
122 contrast,  $\lambda^*$  is a temperature-independent dispersion parameter. The birefringence data for a  
123 wavelength of 550 nm are calculated using the software developed in the laboratory and the  
124 results obtained are plotted in Fig. 2.

### 125 **2.4. X-ray diffraction**

126 Simultaneously small and wide-angle X-ray Scattering (SAXS/WAXS) experiments were  
127 carried out at station I 22 of the Diamond Light Source. The samples are inserted in 1mm  
128 diameter glass capillary and is placed in a magnetic cell of field strength of ~0.5 Tesla in the  
129 horizontal direction placed on the top of a Linkam heating stage for temperature control. The  
130 X-ray wavelength used was 1.0 Å and 2D SAXS/WAXS patterns respectively were collected  
131 with two Pilatus detectors.

### 132 **2.5. Dielectric Spectroscopy**

133 Dielectric relaxation measurements over a frequency range 1 Hz–10 MHz were made using  
134 broadband Alpha High Resolution Dielectric Analyzer (Novocontrol GmbH, Germany). The  
135 glass substrates coated with a low sheet resistance (5 Ω/□) ITO electrodes were used to make  
136 cells. The reason for the low sheet resistance is that peak frequency arising from the sheet  
137 resistance of ITO in series with the capacitance of the cell is shifted to a frequency much higher  
138 than 1 MHz. A prior measurement of the capacitance of the empty cell is made. The  
139 measurement is carried out under the application of weak voltage 0.1V applied across the cell.

140 The temperature of the sample is stabilized to within  $\pm 0.05$  °C. The dielectric spectra are  
 141 analyzed using Novocontrol WINDETA program.

## 142 2.6. Electrical Measurements

143 An electric signal from Agilent 33120A signal generator amplified by high voltage amplifier  
 144 (TReK PZD700) is applied across the cell. The output signal from the resistive (1 k $\Omega$ ) or  
 145 capacitive (2  $\mu$ F) loads was monitored by a digital oscilloscope.

## 146 3. Results and Discussion

### 147 3.1. Molecular design of materials

148 This paper reports a study of the two newly synthesized phenylpyrimidines: WJ-16 and WJ-18  
 149 (Table 1). Here a fluorophenyl group of DIO is replaced by a narrower pyrimidine group and  
 150 this replacement increases the molecular dipole moments from 9.4 D for DIO to 10.4 D for WJ-  
 151 16.

152  
 153 Table. 1. The chemical structures of molecules WJ-16, WJ-18 and of the prototype DIO with  
 154 the phase transition temperatures determined using polarizing microscopy. The dipole  
 155 moments are calculated using DFT B3LYP/ 3-21G with the Gaussian View 9.0. Here N and  
 156 SmA denote superparaelectric (SPE) nematic and smectic A phases.

157

Name of Compound	Molecular structure	Phases and Transition Temperature (°C)	Dipole Moment (D)
DIO		N <sub>F</sub> 66.8 SmZ <sub>A</sub> 83.5 N 173.8 I	9.4-9.5[7, 31]
WJ-16		Cr 79.3 SmA 110.5 N 198.6 I	10.4
WJ-18		Cr 125.6 N 230 Decomposes	14.8

158

159

160 In WJ-18, the terminal fluoro-group is additionally replaced by the cyano-group. This increases  
 161 its molecular dipole moment from 9.4 D for DIO to 14.8 D. It should be mentioned that this is  
 162 not the highest dipole moment as compared to the giant dipole moment 33.5 D reported in the  
 163 literature [22]. Details of the design, synthesis and chemical characterization of WJ-16 and

164 WJ-18 and their crucial intermediates are given in the supplementary Information (ESI, S1-  
165 S36; S41 gives DFT calculated structures). According to the <sup>1</sup>H-NMR spectroscopic data, WJ-  
166 16 does not contain isomers associated with the substitution pattern of the dioxane group,  
167 recently discussed for DIO. For WJ-18, small presence of the isomers is at the detection limit  
168 of ~1-2% (ESI, S13, S30). [32, 33] The dipole moments of the molecules are calculated using  
169 DFT Gaussian software suite at the B3LYP/ 3-21G (D, P) level. Use of the pyrimidine group  
170 instead of the fluorophenyl motif reduces the steric hindrance to the rotations of groups and it  
171 enables increased  $\pi$ -conjugation of the aromatic fragments, resulting in an increased planarity  
172 of the terminal aromatic rings. On cooling from the nematic phase WJ-16 additionally exhibits  
173 SmA phase. The transition temperatures are given in Table 1. In WJ-18, nematic above the  
174 crystal phase is observed, whereas the compound decomposes prior to reaching its N-Iso  
175 transition temperature. Differential scanning calorimetry (DSC) scanned at 10 °C min<sup>-1</sup> on  
176 heating shows WJ-16 melting at 119.5 °C into the LC state, and it then transforming to the  
177 isotropic phase at 200.1 °C, with a transition enthalpy ( $\Delta H$ ) of 0.66 Jg<sup>-1</sup> (0.21 kJmol<sup>-1</sup>) (Figure  
178 S37, ESI). On cooling, a liquid crystalline phase emerges at 199.0 °C ( $\Delta H$ : -0.67 J g<sup>-1</sup>; -0.33 kJ  
179 mol<sup>-1</sup>). A thermodynamically unstable (monotropic) additional LC phase emerges at 111.1 °C  
180 ( $\Delta H$ : -0.22 J g<sup>-1</sup>; -0.21 kJ/mol), prior to crystallization. WJ-18 shows the phase transition from  
181 the N to the crystalline state at 119.8 °C (Figure S38, ESI). Since the dipole moments of  
182 molecules are increased significantly as compared to DIO, dielectric permittivity for both WJ-  
183 16 and WJ-18 becomes colossal as discussed below.

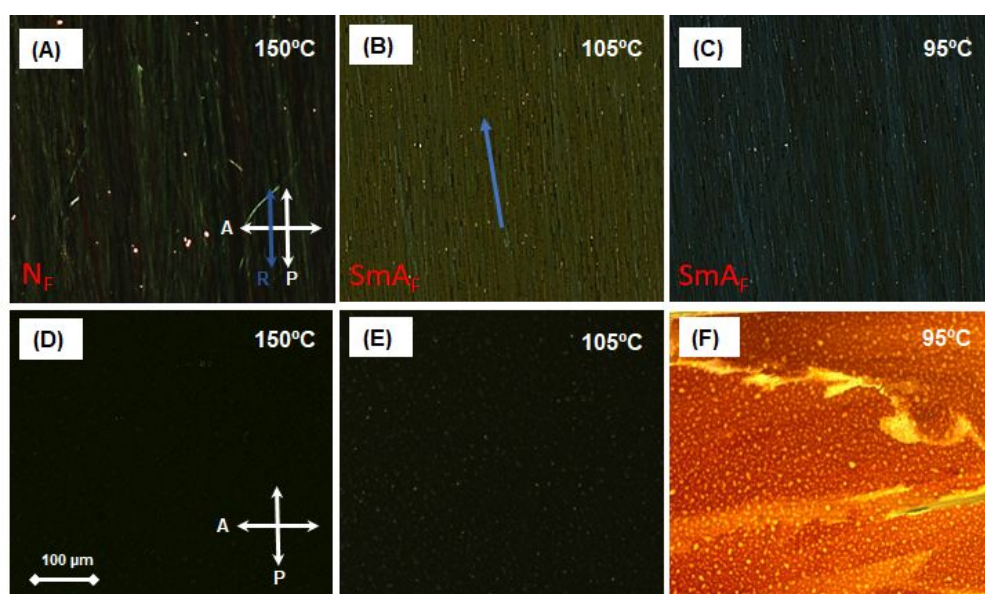
184

### 185 **3.2. The Optical Textures of Liquid crystalline phases.**

186 For investigating the optical textures, we use commercial (E.H.C. Co. Ltd. Japan) and  
187 laboratory fabricated “uncoated” ITO electrodes cells of thicknesses varying from 2 to 25  $\mu\text{m}$ ,  
188 The planar/homeotropic alignment is achieved depending on the alignment layer put on to the  
189 cell electrodes. Fabrication of the cells in the laboratory involves spin-coating surfactant on the  
190 ITO surfaces of substrates. The handmade uncoated cells (i.e. without alignment layers, i.e.  
191 bare electrodes) are also used. Fig. 1 shows the textures obtained from polarizing optical  
192 microscopy (POM) of 9  $\mu\text{m}$  cell filled with WJ-16 under different alignment configurations.

193 Textures of the planar aligned cells, where the rubbing direction (R) makes an angle  
194 of  $\alpha = 45^\circ$  with the polarizer/analyzer (P/A) axis, are identical both in the nematic and the  
195 smectic phases except for a change in the color (Figure S39, ESI). This arises mainly from  
196 a large increase in the birefringence that occurs at the N-SmA transition temperature, under

197 cooling. Some differences in the optical textures in the N and SmA phases are observed as  
 198 the cell is rotated by a small angle, e.g.  $\alpha \approx 5^\circ$ , the rotation of the axis is indicated by a blue  
 199 arrow drawn in Figure 1B. To explore it further, the POM textures of a planar aligned cell  
 200 were recorded with the rubbing direction nearly parallel to the polarizer axis. Here, the  
 201 observed texture in the N phase (Fig. 1A) highly fluctuates and is without domains – a typical  
 202 feature of the conventional nematics. While the texture in SmA phase is non-fluctuating but  
 203 has well defined domains (Figs. 1 B, C). These are the two typical features of smectics. It  
 204 is worth noticing that textures of the parallel rubbed cells do not show ‘twisted domains’ -  
 205 characteristically found in ferroelectric [34,35] nematic phase ( $N_F$ ) of DIO, but the texture  
 206 appears domain-less rather like that of the ordinary nematics.

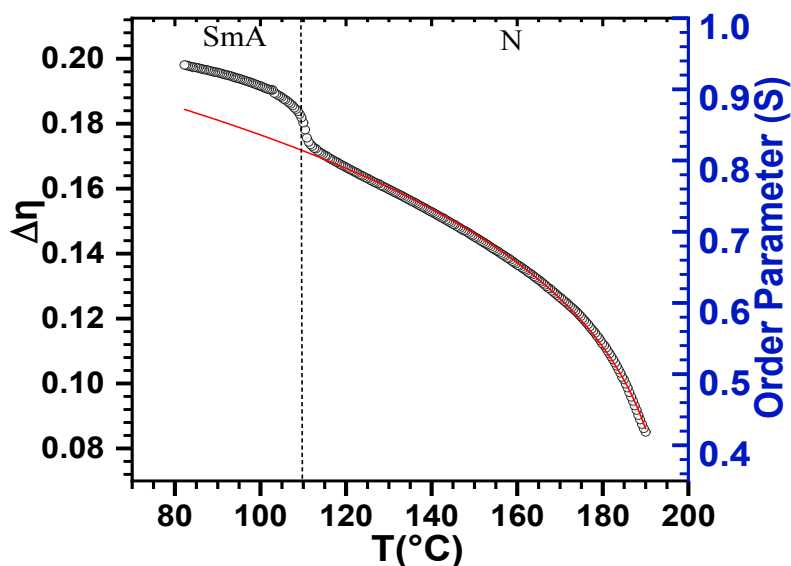


207  
 208 **Figure 1.** The POM textures of a homogeneously aligned planar cell (A-C) filled with  
 209 **WJ-16** with the rubbing direction (in blue) lying parallel to the polarizer, and bare ITO  
 210 cell using the same compound (D-F) at temperatures of 150 °C, 105 °C, and 95 °C.  
 211 Here A and P refer to the analyzer and the polarizer, and R in blue refers to the rubbing  
 212 direction in a planar aligned cell. The scale bar shown in 2D is of the length 100  $\mu\text{m}$ .  
 213

214 Both WJ-16 and WJ-18 filled in commercial homeotropic cells show perfect  
 215 homeotropic texture, in contrast to the texture of the  $N_F$  phase of DIO [7,1911] where the partial  
 216 *Schlieren* texture is observed in a homeotropic aligned cell. WJ-16 when filled in uncoated  
 217 cells ( i.e.using bare ITO electrodes) shows perfect homeotropic texture with a large  
 218 extinction in the nematic and SmA phases (Figures 1D, E). On further cooling the sample  
 219 cell to a temperature of 95 °C, the texture transforms to that of a non-homogeneous planar  
 220 cell (Figure 1F). This fortuitous property of obtaining homeotropic texture with bare  
 221 electrodes allows us to record the dielectric spectra in homeotropic configuration without  
 222 alignment layers. This is advantageous since the alignment layers may introduce uncertainty

223 in the measurements of complex dielectric permittivity. WJ-18 displays only the nematic  
 224 phase. However, in the uncoated cells, WJ-18 unlike WJ-16 does not show homeotropic  
 225 alignment but gives non-homogenous planar texture (Fig. S40, ESI). We note that the  
 226 isotropic phase of WJ-18 is unreachable due to its thermal decomposition occurring at a  
 227 temperature of 230 °C.

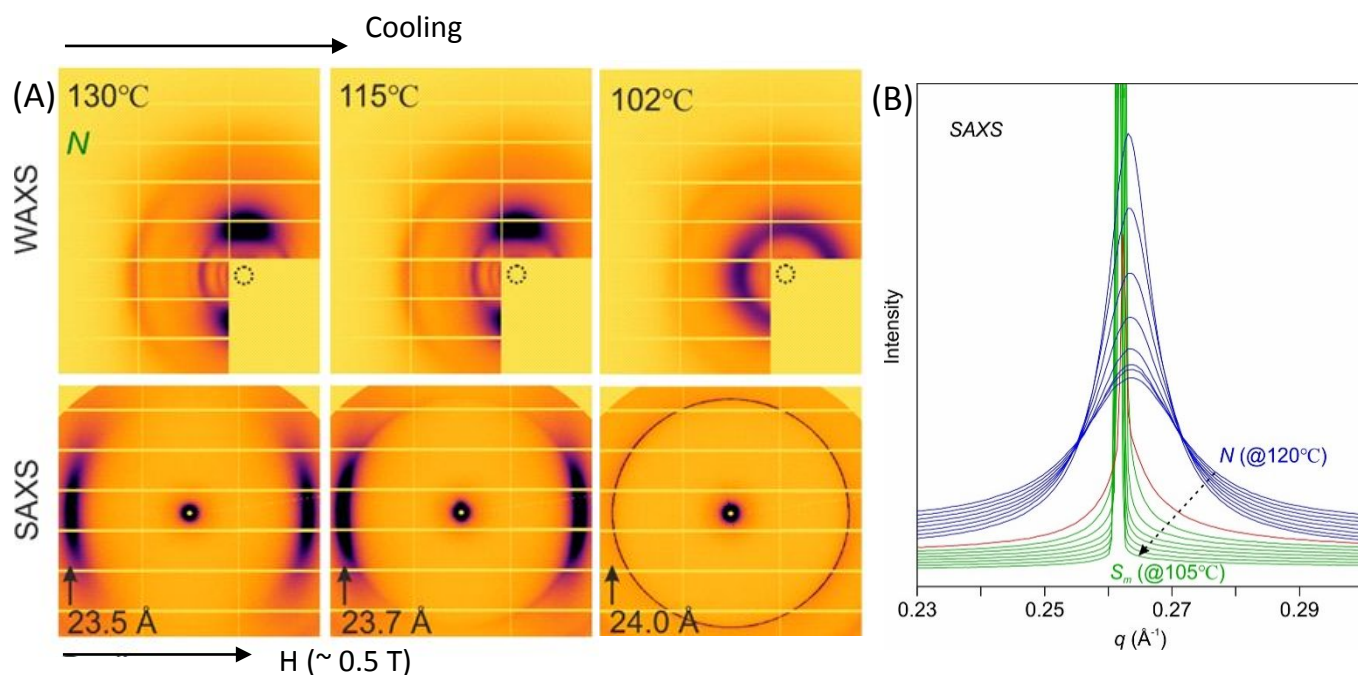
228 To characterize the LC phases, the birefringence of WJ-16 is measured in a planar-  
 229 aligned cell of 25  $\mu\text{m}$  cell thickness and is calculated for a wavelength of 550 nm. Fig. 2  
 230 shows that the birefringence increases with decreasing temperature, and a significant step  
 231 increase in birefringence occurs at the N to SmA transition temperature is observed. The  
 232 behavior of these phases relates to the observed increase in the nematic order parameter  $S$ .  
 233 This is verified by fitting the birefringence data to the empirical Haller equation [36] (shown  
 234 as red line in Fig. 2) with  $S_{\Delta T} = S_0(\Delta T)^\gamma$ , where  $\Delta T = T_{N-iso} - T$ ,  $\gamma = 0.25$ . On using the wide-  
 235 angle X rays scattering (WAXS) set-up where the sample alignment is achieved by external  
 236 magnetic field, we obtain  $\gamma = 0.28$  [Figure S42, Supplementary Information]. At the N to  
 237 SmA phase transition temperature, the orientational order parameter increases significantly  
 238 by as much as 0.16. This is a much larger step increase in the order parameter compared to  
 239 the calamitic and bent-core LC systems reported in the literature. A comparison of the plots  
 240 of the birefringence vs. temperature for WJ-16 with DIO shows that only a single nematic  
 241 phase exists in WJ-16 unlike DIO, where more than one nematic phase is observed.



242  
 243 **Figure 2.** The birefringence ( $\Delta n$ ) plot of **WJ-16** (with scale on the left Y-axis) and the  
 244 order parameter (scale on the right Y-axis) as a function of temperature for a wavelength  
 245 of  $\lambda = 550$  nm obtained using a homogeneous planar aligned 25  $\mu\text{m}$  thick cell. The red thin  
 246 line is a fit of the Haller's equation to the birefringence data. Interestingly a significant  
 247 increase in the order parameter ( $\sim 0.16$ ) occurs at the N to SmA transition temperature.  
 248

### 249 3.3. X-ray diffraction Study

250 To characterize the nanoscopic assembly behavior of WJ-16, small (SAXS) and wide angle  
 251 (WAXS) X-ray scattering studies are carried out on magnetically aligned samples using  
 252 synchrotron radiation. The nematic phase observed at temperatures between  $\sim 200$  °C and 111  
 253 °C is characterized by a broad, but well oriented scattering peaks observed in both the small  
 254 and the wide-angle regions (Figure 3A). The SAXS peak maxima lies in the horizontal  
 255 direction, i.e., along the direction of the magnetic field. These observations indicate the  
 256 average distance between the centers of molecules is 23.5 Å at 130 °C which is close to the  
 257 molecular length found from molecular modelling (24 Å) and is consistent with the expectation  
 258 that the molecular axes are oriented along the field direction. The main WAXS peak is  
 259 observed in the vertical direction, with a corresponding  $d$ -spacing of  $\sim 4.5$  Å. This again is  
 260 consistent with the expected average distance between the molecules in the lateral direction.  
 261 On cooling from the nematic phase, a sharp Bragg diffraction peak is observed at a temperature  
 262 of  $\sim 111$  °C, arising from a formation of the smectic phase. On further cooling, the sample goes  
 263 to the crystalline state where multiple sharp Bragg peaks are seen in both SAXS/WAXS  
 264 regions. The SAXS peak of the smectic phase has a corresponding  $d$ -spacing of 23.9 – 24.1 Å  
 265 ( $q \sim 0.262$  Å<sup>-1</sup>). This again agrees with the molecular length, and it confirms that the phase is  
 266 of SmA type, i.e., the average direction of the molecules is parallel to the smectic layer normal.



267  
 268 **Figure 3.** (A) Simultaneous SAXS/WAXS patterns of phases formed by **WJ-16** on cooling  
 269 from 140 °C to 85 °C at a rate of 2 °C/min, with  $d$ -spacings of the scattering/diffraction peaks  
 270 marked in SAXS. The WAXS beam center is indicated by a dashed circle, 3(B) 1D plot of

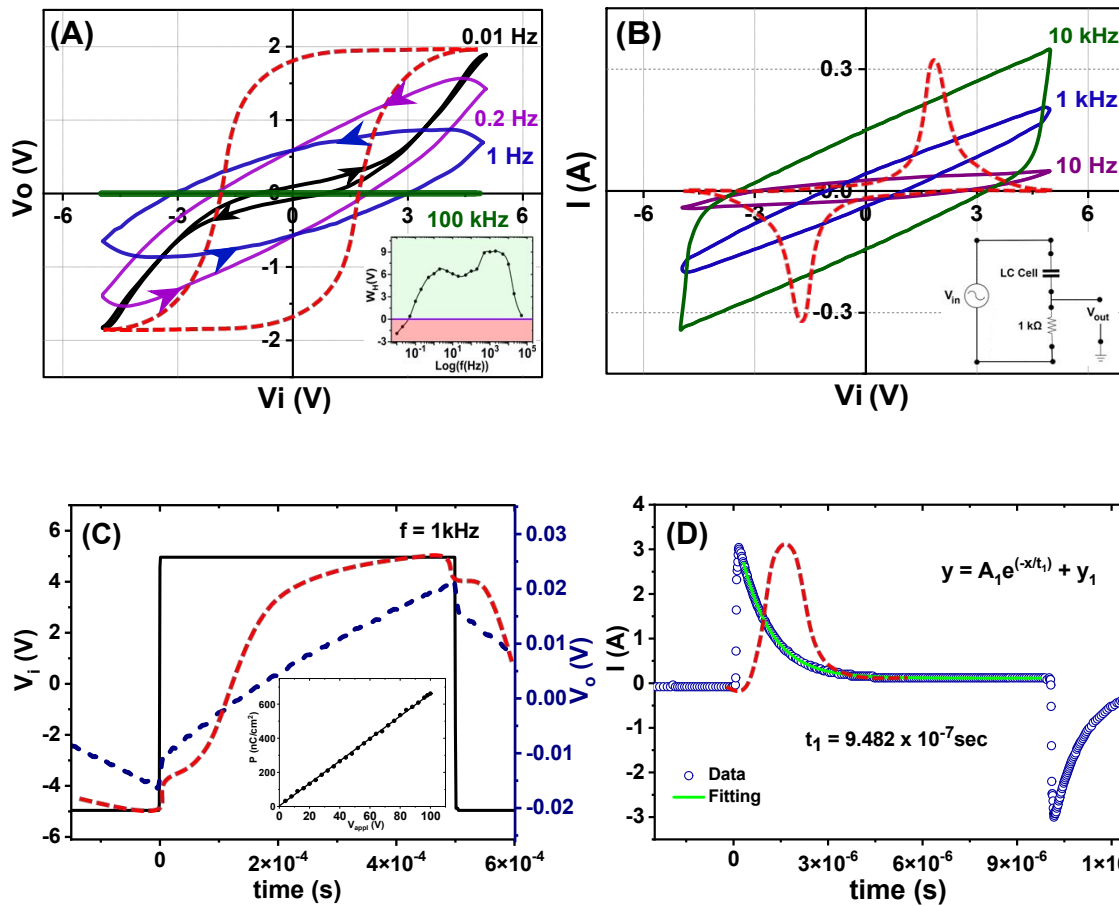
271 the SAXS intensities as a function of  $q$  for different temperatures (120 -105 °C), N is indicated  
272 in blue, SmA in green, the phase transition temperature N -SmA is shown in red.

273 The distinct sharpening of the small angle scattering peak with decreasing temperature  
274 at the transition from the N to SmA is shown in Figure 3B. The  $d$ -spacings observed in the N  
275 phase of WJ-16 are like those observed for DIO [7]. On the basis of the FWHMs of the SAXS  
276 and the WAXS peaks, we calculate the correlation lengths in the nematic phase both in  
277 longitudinal and lateral directions. The lateral correlation length is essentially constant in the  
278 entire N phase ( $\sim 3.2$  Å), thus confirming the liquid-like short range positional order of N-phase.  
279 However, the longitudinal correlation length decreases, first rapidly just above the SmA phase,  
280 from  $\sim 210$  Å at 116 °C to  $\sim 100$  Å at 122 °C, but then slowly to  $\sim 50$  Å at 150 °C and  $\sim 23$  Å  
281 (single molecular length) just prior to the occurrence of the N-Iso transition (Figures. S43 and  
282 S44, ESI). The observed simultaneous SAXS/WAXS patterns of WJ-18 confirm formation of  
283 the N phase between the crystalline and the isotropic states. The SAXS peak has  $d$ -spacing of  
284  $\sim 25.0$  Å, almost the same as the length of WJ-18 molecule. The wide angle scattering in the  
285 vertical direction centers around 4.7 Å, suggesting a slightly larger side-way distance in the N  
286 phase. On heating the crystalline sample melts at  $\sim 180$  °C, whereas on cooling it crystallizes  
287 at 130 °C at the rate of 2 °C/min. (Figures. S45 and S46, ESI)

### 288 **3.4. Electrical study and discussion of the hysteresis in $P$ vs. $E$**

289 The main objective of the molecular design was to enhance its dipole moment and to increase  
290 the dielectric permittivity to understanding the structure-property relationships and its  
291 correlation to the ferroelectric nematic phase in the related material such as DIO. We  
292 examined ferroelectric behavior or its absence in WJ-16 and WJ-18 through studies of the  
293 hysteresis in the polarization  $P$  vs.  $E$ . A conventional method of measuring the polarization  
294 as a function of  $E$  is using the Sawyer-Tower circuit [37,38]. In this circuit, sample is connected  
295 in series with a capacitor of a known value thus forming the capacitor divider electrical circuit.  
296 To obtain whether hysteresis in  $P$  vs.  $E$  is present, output of the capacitor divider circuit is  
297 connected to the Y-input, whereas the applied triangular voltage is connected to X-input in  
298 the X-Y mode of the oscilloscope. Figures 4A and 4B show electrical responses of the sample  
299 to applied triangular wave voltage signal of 100  $V_{pp}$ , (subscript 'pp' to V stands for the peak-  
300 to-peak voltage) using (A,C) the capacitive and (B,D) the resistive circuits (the latter circuit  
301 is shown in the inset of Fig. 4B).

302



303

304

305 **Figure 4.** The capacitive (A) and the resistive (B) response of WJ-16 filled 9  $\mu\text{m}$  uncoated  
 306 cell at 150  $^{\circ}\text{C}$  for different frequencies, 100  $V_{\text{pp}}$  triangular voltage is applied (in the X-Y  
 307 mode) of the oscilloscope. The inset in Figure 4A shows variation of the measured  
 308 hysteresis width ( $W_{\text{H}}$ ) as a function of frequency of the applied signal; (C) and (D)  
 309 correspond to the recorded voltages across the capacitor ( $V_{\text{O}}$ ) and the current ( $I$ ) through  
 310 the resistance on the application of 100  $V_{\text{peak to peak}}$  square voltage, connected to the  
 311 oscilloscope in Y-t mode. Here, the red dashed lines correspond to anticipated ferroelectric  
 312 hysteresis response, whereas the blue dash lines in C correspond to the actual voltage  
 313 response and the blue data points in Fig 1 D represent the observed current response. Green  
 314 line is a fit to the equation given in the inset of Fig. 4D.

315

316 Shape of the response curves can be considered “pseudo-hysteresis”, i.e., the polarization  
 317 lags behind electric field since the negative and the positive slopes do not match with each  
 318 other. Furthermore, a saturation of  $P$  with  $E$  is not exhibited. The proof of the real classical  
 319 hysteresis behavior is that saturation in the polarization  $P$  with  $E$  is observed, just like a dashed  
 320 curve in Figure 4A. In our case, shape of the experimental response curve is far removed from  
 321 the normal hysteresis curve (observed for DIO [7]). Shapes of such pseudo-hysteresis curves  
 322 are strongly dependent on the frequency of the applied field, and these can easily be explained  
 323 by the dynamic lag of the electric field [39]. It is to be noted that problem of finding the ‘static  
 324 hysteresis loop’ experimentally is a challenging task and it was studied in detail in Ref. [40].

325 Firstly, the hysteresis loop width (the double coercive voltage) shows dynamic increase with  
326 frequency due to the dynamic delay in switching,<sup>[39]</sup> hence the frequency for a given applied  
327 field must be sufficiently low. Therefore, even with the absence in the saturated polarization,  
328 the dynamic curves can easily be denoted as the “pseudo-hysteresis” with hysteresis-like  
329 response. Secondly, the hysteresis width (or the double coercive force) continues to vary  
330 evenly in the low and ultra-low frequency ranges: from 1 Hz down to  $10^{-4}$  [40] due to the  
331 screening effect arising from electronic charges due to the impurities that accumulate on the  
332 interface between the alignment layer and the dielectric medium. This effect explains the  
333 inverse (negative) hysteresis loop observed at very low frequencies of 0.01 and 0.2 Hz (Figure  
334 4A). Hence we conclude no real ferroelectric hysteresis is observed in our samples. This is  
335 additionally confirmed by measuring the response using the resistive load (Figure 4B).  
336 Ferroelectric switching must lead to two distinctive peaks<sup>[41]</sup> as shown by dashed lines in  
337 Figure 4B. We do not observe these peaks for WJ-16 and WJ-18, thus proving that the  
338 switching behavior is not ferroelectric. In ferroelectric nematic phase of DIO, two current  
339 peaks are clearly visible in the  $N_F$  phase [7].

340 An alternative method of measuring the spontaneous polarization, using the circuit with  
341 the capacitive<sup>[42]</sup> and the resistive [9] loads, is to monitor the response across the load to the  
342 applied square-wave voltage in time domain (i.e., using the Y-t mode of the oscilloscope). This  
343 allows for simultaneous measurements of both the switching time and the rotational viscosity.  
344 Figures 4C and 4D show the observed voltage and the current responses using the capacitive  
345 ( $2 \mu\text{F}$ ) and the resistive ( $1 \text{ k}\Omega$ ) loads. Instead of the characteristic waveform obtained for  
346 ferroelectricity (shown by grey-dashed lines) in terms of the smooth voltage peaks arising from  
347 an integration of the re-polarization current<sup>[42]</sup>, we observe classical paraelectric waveform.  
348 Similarly, for the resistive circuit, we expect the output to be Gaussian reported by Chen *et. al.*  
349<sup>[9]</sup>. However, we observe only the exponential decay of the current but without the elongation  
350 of the pulse, a typical response from a conventional nematic LC.

351 Another way to check whether it is ferroelectric or not is to examine the dependence of  
352  $P$  on  $E$ . The inset in Fig.4 shows the dependence of electrical displacement in  $4 \mu\text{m}$  planar  
353 WJ-16 cell on applied sine-wave voltage. One may see that that this dependence is perfectly  
354 linear in both ways: on increasing and decreasing the applied amplitude voltage up to 100 V  
355 ( $25 \text{ V}/\mu\text{m}$ ) at which the induced polarization is  $\sim 0.7 \mu\text{C}/\text{cm}^2$ . We can estimate how far it is  
356 away from saturation. Assuming a typical (for such a large dipole moment) value of the  
357 spontaneous polarization  $\sim 5 \mu\text{C}/\text{cm}^2$  [11,12], the expected saturation will occur at 500 V or  
358 higher. Hence, for the practical voltage applied, the P-E response is paraelectric-like.

359 The second harmonic generation (SHG) experiments are performed on these samples.  
 360 Unlike ferroelectric nematic phases [7] the SHG signal was not observed, this confirmed the  
 361 absence of ferroelectricity.

362 Summarizing, neither the hysteresis in P vs. E nor any other ferroelectric property was  
 363 observed in the entire liquid crystalline temperature range of both WJ-16 and WJ-18.

### 364 **3.5. Dielectric spectroscopy**

365 In contrast to our expectations, both materials do not show presence of ferroelectricity in  
 366 POM, P-E and SHG studies however they do show CP. To study the physical origin of this  
 367 phenomenon we used the technique of dielectric spectroscopy, one of the most sensitive  
 368 techniques for studying ferroelectric and other polar materials/phases. This was successfully  
 369 employed for characterization of the ferro-[<sup>43,44,45,46</sup>] / antiferro- [<sup>47,48</sup>] and ferri-electric [<sup>49,50</sup>]  
 370 liquid crystalline phases. Dielectric spectroscopy of WJ-16 and WJ-18 are investigated using  
 371 Novocontrol high precision Impedance Alpha analyzer, employing initially commercial cells  
 372 of different thicknesses with both homeotropic and planar alignments. The dielectric spectra  
 373 were recorded in the frequency range of 0.1 Hz to 10 MHz with 0.1 V measuring AC voltage.  
 374 The complex permittivity data were fitted to the Havriliak-Negami, eqn. (1) below, where the  
 375 DC conductivity term is also included [<sup>51</sup>]:

$$376 \quad \varepsilon^* = -\frac{i\sigma}{\varepsilon_0\omega} + \varepsilon_\infty + \sum_{j=0}^n \frac{\Delta\varepsilon_j}{[1+(i\omega\tau_j)^{\alpha_j}]^{\beta_j}} \quad (1).$$

377 Here  $\varepsilon^*$  is the complex permittivity and  $\varepsilon_\infty$  is the high frequency permittivity. The latter  
 378 includes electronic and atomic polarizabilities of the material.  $\omega$  is the angular frequency of  
 379 the probe field,  $\varepsilon_0$  is the permittivity of free space,  $\sigma$  is the DC conductivity,  $\tau_j$  is the relaxation  
 380 time,  $\Delta\varepsilon_j$  is the dielectric strength of the  $j^{\text{th}}$  relaxation process,  $\alpha_j$  and  $\beta_j$  are the corresponding  
 381 symmetric and the asymmetric broadening parameters of the distribution of relaxation times.

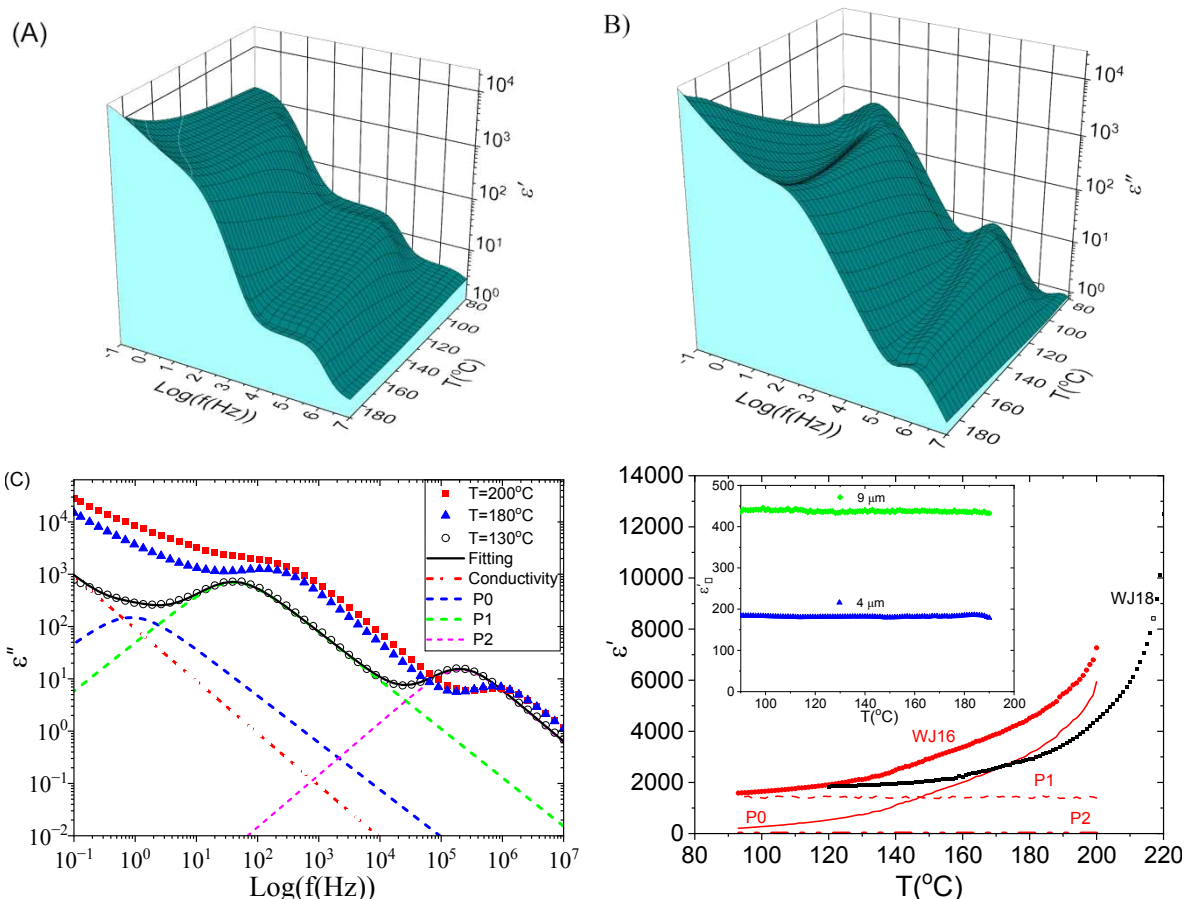
382 Initially the measurements were made using commercial cells with planar alignments.  
 383 Figure 5D (Inset) shows temperature dependencies of the total dielectric permittivity (i.e. real  
 384 part of complex permittivity,  $(\varepsilon')$  using 4  $\mu\text{m}$  ( blue filled triangle) and 9  $\mu\text{m}$  ( green filled  
 385 diamond)) planar aligned cells. WJ-16 shows significantly large values of the dielectric  
 386 strength ( $\sim 200$  and  $\sim 450$ ) which could possibly be associated with ferroelectricity. However,  
 387 it should be noted that the dielectric spectra of WJ-16 are different from the ferroelectric DIO  
 388 material [<sup>52</sup>]. The dielectric permittivity WJ-16 is temperature independent in the entire  
 389 temperature range, while the DIO shows temperature dependent soft-mode like behavior in

390 non-ferroelectric phases (N, SmZ<sub>A</sub>) and temperature independent permittivity in the  
 391 ferroelectric nematic phase, N<sub>F</sub>. The independence of the permittivity on temperature shown  
 392 in Fig. 5D is rather ‘unusual behavior’ and this requires further investigation. Recently, the  
 393 Boulder group (N. Clark et al.) found the effect of insulating alignment layers on the  
 394 apparent/measured values of the dielectric permittivity [15]. In this case, the apparent  
 395 capacitance  $C_{app}$  of LC cell can be expressed as two capacitances in series: the capacitance of  
 396 the LC layer  $C_{LC}$  and capacitance of  $C_I$  of insulating alignment layer. Hence the apparent  $C_{app}$   
 397  $= \frac{C_{LC} \cdot C_I}{C_{LC} + C_I}$ . There can be two possible opposite cases: the ordinary case where  $C_{LC} \ll C_I$  and the  
 398 extraordinary case, where  $C_{LC} \gg C_I$ . In the ordinary one, i.e., in materials with the low/moderate  
 399 dielectric permittivity, capacitance of the LC cell  $C_{LC} \ll C_I$  and the apparent capacitance is the  
 400 capacitance of LC cell,  $C_{app} = C_{LC}$ . Hence, in the ordinary case, this gives real value of  
 401 capacitance and permittivity. However, in materials with very high dielectric permittivity ( $\epsilon >$   
 402 10,000), such as the ferroelectric N<sub>F</sub> phase and bent-core LCs [53,54] the capacitance of LC cell  
 403 can easily exceed the capacitance of the alignment layer,  $C_{LC} \gg C_I$ . In such a case, the apparent  
 404 capacitance is limited by the capacitance of the insulating layers,  $C_I$ . We term it as the “Clark’s  
 405 limit”,  $C_{app} = C_I$ . In our case however called extraordinary, the apparent  $C(T)_{LC} \gg C_I$ , the LC  
 406 capacitance (and dielectric permittivity) would be limited by Clark’s limit  $C_I$  which is a  
 407 constant over a reasonable range of temperatures.

408 Another important feature of the extraordinary case is that the apparent capacitance will  
 409 be linearly dependent on the cell thickness [15]. Both features of the extraordinary case are  
 410 supported by the results given in Fig. 5D. We can estimate the capacitance of the insulating  
 411 alignment layers of our cells  $C_I = \frac{\epsilon_I \epsilon_0 A}{2d_I}$ , and assuming the layer thickness  $d_I = 200$  nm, and its  
 412 permittivity as  $\epsilon_I \sim 5$ , we obtain  $C_I \sim 5.5$  nF. This capacitance limits the apparent value of the  
 413 dielectric permittivity for the 4  $\mu$ m cell to 100, in good agreement with the experimental value  
 414 of 180, considering that the assumed values of thickness and permittivity of the alignment layer  
 415 may be different from the actual values. To avoid this limitation and to get the actual values  
 416 of the dielectric permittivity, one needs to increase the capacitance of the alignment layers  $C_I$   
 417 in approaching the ordinary case  $C_I \gg C_{LC}$ . The only way to achieve this is to reduce their  
 418 thicknesses or simply use the uncoated metal/ITO electrodes as already used in some works  
 419 reported in the literature [11,13,14,16,27, 55] and this allows us to measure the permittivity up  
 420 to 50,000.

421 Following this approach, we performed the dielectric measurements of both WJ-16 and  
 422 WJ-18 using handmade 4  $\mu$ m cells with bare ITO electrodes. Figures 5 (A) and 5(B) show a

423 three-dimensional (3D) plot of the real and imaginary parts of dielectric permittivity of 4  $\mu\text{m}$   
 424 WJ-16 uncoated cell. Figure 1(C) shows the dielectric loss spectra for uncoated 4  $\mu\text{m}$  WJ-16  
 425 cell taken at temperatures of 130, 180 and 200  $^{\circ}\text{C}$  with the corresponding fitting at 130  $^{\circ}\text{C}$  and  
 426 (D). The temperature dependence of the total dielectric permittivity of the uncoated 4  $\mu\text{m}$  cells  
 427 WJ-16 and WJ-18.



428

429

430 **Figure 5 (A) and (B)** show three-dimensional (3D) plot of the real and imaginary parts of  
 431 dielectric permittivity of WJ-16 4  $\mu\text{m}$  cell with bare ITO electrodes; **(C)** shows the  
 432 frequency dependence of the imaginary part of permittivity at a temperature of 111  $^{\circ}\text{C}$ ;  
 433 circle symbols,  $\circ$ , denote the experimental data, the solid black line is a fit to Eq. 1, while  
 434 the blue, green and magenta dashed lines denote P0 (the electrode polarization process),  
 435 relaxation processes P1 and P2, while the red dashed straight line with a slope of -1  
 436 represents the DC conductivity; **(D)** Temperature dependence dielectric permittivity for  
 437 two 4  $\mu\text{m}$  uncoated cells for WJ-18 ( $\blacksquare$ ) and WJ-16 ( $\bullet$ ) and dielectric strengths of three  
 438 individual relaxation processes P0 (solid red line), P1 (dashed red) and P2 (dot-dash). **Inset**:  
 439 Temperature dependence dielectric permittivity of two WJ-16 planar 4  $\mu\text{m}$  ( $\blacktriangle$ ) and 9  $\mu\text{m}$   
 440 ( $\diamond$ ) cells  
 441

442 A comparison of the temperature dependencies of the total dielectric permittivity of 4  $\mu\text{m}$   
 443 planar aligned cell (Fig. 5D) and uncoated 4  $\mu\text{m}$  cells (Fig. 5D) of WJ-16 shows that the  
 444 dielectric strength of uncoated cell is about one order higher than of the planar aligned cell and  
 445 it becomes temperature dependent. These two features reflect that the Clark's limit is avoided

446 in the bare electrodes cell and the measured values should reflect the real value of the dielectric  
447 permittivity. One may note that in uncoated cells the dielectric permittivity is increasing with  
448 temperature and reaches maximal values in the isotropic phase. To understand this unusual  
449 feature, we focus on the individual relaxation processes which contribute to the total dielectric  
450 permittivity.

451 Figure 5C is an example of the fitting of the dielectric loss spectra to three relaxation  
452 processes at 130 °C. These are named as P0, P1 and P2 with increase in the relaxation  
453 frequency. During the fitting of the spectra to Eqn. (1) both stretching parameters ( $\alpha$ ,  $\beta$ ) were  
454 initially not fixed for all processes. On fitting we obtain  $\alpha=1$  and  $\beta=1$  for both P1 and P2. The  
455 stretching parameters values of unity imply that the relaxation processes are pure Debye.  
456 Normally in the conventional calamitic liquid crystals, there exist two individual relaxation  
457 processes, one around the short axis often called the ‘flip flop mode’ (observed at lower  
458 frequencies) and the second rotation around the long molecular axis (exhibited at higher  
459 frequencies). Since the dielectric strength of P1 is found to be much higher in homeotropic  
460 (not discussed in the present manuscript) than in planar-aligned cell, process P1 can be assigned  
461 to flip-flop mode and P2 correspond to the rotations around the long molecular axis, as reported  
462 in the literature [20,52,56]. The stretching parameter,  $\alpha_0$ , for P0 lies in the range 0.65 - 0.9  
463 depending on the temperature. Here P0 is assigned to the parasitic ionic relaxation dynamics,  
464 caused by the separation of positive and negative charges, their motions in opposite directions  
465 end by their accumulation on the two electrodes. The process P0 in the dielectric loss spectra  
466 is broadened and hence  $\alpha < 1$ . In other words, P0 is assigned to the space charge/interfacial  
467 polarization produced by the mobility of ions and finally to their accumulation on the  
468 electrodes.

469 Now we can explain the huge dielectric permittivity in the isotropic phase. Fig. 5(D)  
470 shows the temperature dependencies of the total dielectric permittivity using 4  $\mu\text{m}$  uncoated  
471 cells for WJ-16 (red filled circle) and WJ-18 (black filled square) and the dielectric strength of  
472 processes P0 (solid red line), P1 (dashed red line) for WJ-16 which contribute mostly to the  
473 total dielectric permittivity. The parasitic ionic process P0 is strongly temperature dependent,  
474 while P1 is almost independent of temperature. At lower temperatures  $\Delta\epsilon_1 \gg \Delta\epsilon_0$  and the  
475 total dielectric permittivity is also almost temperature independent. However, the dielectric  
476 strength  $\Delta\epsilon_0$  of P0 grows quickly with temperature and at  $\sim 152$  °C it exceeds the dielectric  
477 strength  $\Delta\epsilon_1$  and contributes mostly to the total permittivity. Therefore, the huge dielectric  
478 permittivity in high temperature range, including the isotropic phase is obviously due to the

479 parasitic ionic process. A similar observation and explanation of the CP in isotropic phase was  
480 given by [57,58]

481 Now by ignoring the parasitic ionic process P0 let us examine the relaxation process P1  
482 in greater detail. Most striking feature of this process is a CP (~1,500) which is independent  
483 of temperature and phase but linearly depends on the cell thickness, i.e dielectric strengths in  
484 4, 9, 22  $\mu\text{m}$  cell are 1500, 3000, 7000 correspondingly. The magnitude of dielectric strength  
485 of P1 is two-three orders of magnitude higher than in paraelectrics and about one order smaller  
486 than the Goldstone mode in ferroelectric nematics [7,8,26,27,31,56] and some bent-core LCs  
487 [53,54]. In these ferroelectric materials the dielectric strength strongly depends on bias voltage  
488 which suppresses the Goldstone mode [13,15,54,]. However our samples unlike ferroelectric  
489 materials show paraelectric-like, hysteresis free linear P-E response and this property together  
490 with the CP can be assigned to SPE which appears in the temperature range of the paraelectric  
491 and ferroelectric phases [59] In contrast to ferroelectric nematics the dielectric spectra of our  
492 materials do not depend on bias voltage due to the absence of the spontaneous polarization.

493 High dielectric permittivity very likely reflects extremely strong collective molecular  
494 dipolar contribution. In the solid state, SPE arises from well-aligned molecular clusters which  
495 also exist in bent-core LCs [53,54]. However, in our materials such clusters were not observed  
496 and the CP can be explained by response of the correlated conglomerates of molecules. The  
497 possible physical mechanisms will be discussed later.

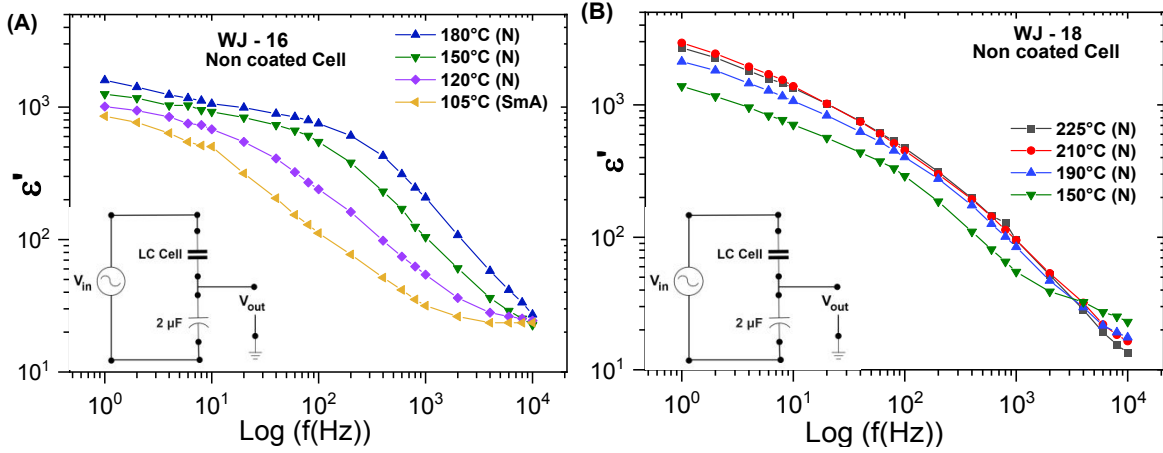
498 Since results of the permittivity measurements by dielectric spectroscopy are currently  
499 hotly debated [14,15,17], to validate the obtained permittivity values, we use the direct  
500 capacitance measurements to support observation of the colossal permittivity CP.

501

### 502 **3.6. Direct capacitance measurements.**

503 The colossal dielectric permittivity (CP) obtained by dielectric spectroscopy of uncoated cells  
504 can be confirmed by direct capacitance measurements of the LC sample. By definition,  
505 dielectric permittivity,  $\epsilon'$  is a ratio of capacitances of the filled and empty cell, so the direct  
506 capacitance measurements will give most reliable value for capacitance and permittivity  
507 irrespective of any physical model. We used a capacitor divider circuit, shown in the inset  
508 of Figure 7, the capacitive load,  $C_0 = 2 \mu\text{F}$ . The capacitance of LC sample is measured as  $C_{LC}$   
509  $= C_0 \frac{V_0}{V_{in} - V_0}$ , the real part of the permittivity is deduced from  $\epsilon'_{LC} = \frac{d \cdot C_{LC}}{\epsilon_0 A}$ . Figures 7A and 7B

510 show frequency dependencies of the dielectric permittivity for different temperatures (SmA,  
 511 N and the Iso phases) using 4  $\mu\text{m}$  uncoated cells of WJ-16 and WJ-18, respectively.



512  
 513

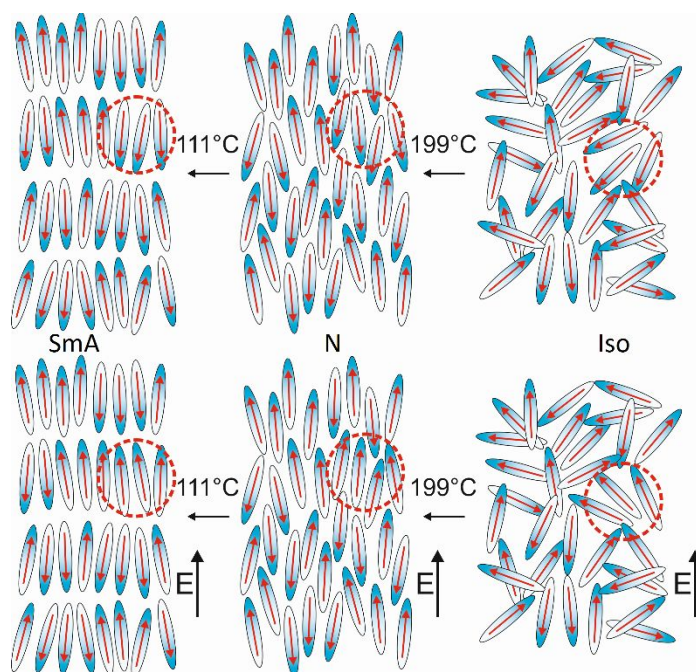
514 **Figure 6.** The direct measurement of dielectric permittivity ( $\epsilon'$ ) as a function of frequency for  
 515 different temperatures using the capacitance voltage divider circuit using uncoated 4  $\mu\text{m}$  cells  
 516 filled with (A) WJ-16 and (B) WJ-18. The inset in figure 6B shows a simple capacitance divider  
 517 circuit used in the measurement of  $\epsilon'$ , where  $V_{in}$  is applied sin-wave voltage and  $V_{out}$  in the output  
 518 voltage taken from 2  $\mu\text{F}$  capacitor.

519

520 It is interesting to note that the frequency dependence of the dielectric permittivity  
 521 calculated from direct capacitance measurements using uncoated cells of both samples (Figure  
 522 7A,B) match with the values measured by dielectric spectroscopy (Figure 5). The result  
 523 demonstrates CP in both the N and SmA phases.

524

525 A direct measurement of the dielectric permittivity provides a clear and direct evidence  
 526 for the observation of colossal dielectric permittivity of non-ferroelectric compounds, WJ-16  
 527 and WJ-18. Hence, this behavior can only be related to superparaelectricity (SPE) [5, 59] in  
 528 soft matter systems. Superparaelectricity reflects an incomplete ferroelectric long-range order.  
 529 Ferroelectric state is an assembly of the long-range-ordered polar domains having spontaneous  
 530 polarization ( $P_s$ ) and it exhibits hysteresis in the polarization as function of the external electric  
 531 field, while the superparaelectric state consists of the short-range polar order clusters. For the  
 532 latter, the macroscopic polarization  $\langle P_s \rangle \sim 0$  and a hysteresis free P-E curve is observed.  
 533 Figure 7 is a schematic of the proposed dipolar structures in WJ-16 for the three phases. Both  
 states, superparaelectric and the ferroelectric, show large dielectric permittivity.



534  
535

536 **Figure 7.** The proposed schematics of dipolar structures and the molecular assembly in  
537 the phase sequence of WJ-16.

538 However, our studied compounds W-16 and WJ-18 exhibit colossal permittivity even in  
539 the isotropic phase with the absence of hysteresis in all phases. Therefore, phases of these  
540 compounds can be assigned superparaelectrics rather than to ferroelectrics. The higher values  
541 of dielectric permittivity can be explained using the classical approach suggested by Kirkwood  
542 and Frohlich, <sup>[60]</sup> where the static dielectric permittivity  $\epsilon_S$  in paraelectric isotropic liquids is  
543 given by:

$$544 \quad \epsilon_S - n^2 = \frac{3 \epsilon_S}{2\epsilon_S + n^2} \frac{N}{3 kT \epsilon_0} \mu \mu^* \quad (2)$$

545  $n$  is the refractive index at a visible wavelength,  $kT$  is the thermal energy,  $\mu$  is the dipole  
546 moment of the molecule,  $\epsilon_0$  is the permittivity of free space.  $\mu^*$  is the average moment of the  
547 dipoles in a macroscopic spherical region surrounding the dipole on the assumption that one of  
548 the dipoles is kept in a fixed direction.  $N$  is the number density of molecules.  $M/d$  is the molar  
549 volume,  $N_A$  is the Avogadro number;  $N \cdot \frac{M}{d} = N_A$  and  $\mu \mu^* = \mu^2 (1 + z \cos \gamma)$ , where  $\cos \gamma$  is  
550 the average of the cosine angle between the neighboring molecules,  $z$  is the average number of  
551 the interacting dipoles, also called the coordination number. Assuming  $\cos \gamma$  equal to unity,  
552 the dielectric permittivity is proportional to the square of the dipole moment and to the  
553 coordination number,  $z$  plus one. A ferroelectric copolymer with the permittivity of 130 has a

554 coordination number of 30 [61], while the coordination number of 1000 was reported in a bent  
555 core compound [54].

556 In solid state SPE systems, dielectric permittivity is temperature dependent because it  
557 depends on the size of ferroelectric domains/clusters but not on the size of the sample. Contrary  
558 to this the dielectric strength of a ferroelectric LC is proportional to the thickness of the cell  
559 and this observed in different phases such as surface-stabilized SmC\* [46], bent-core LCs [54]  
560 and ferroelectric nematic N<sub>F</sub> [15,16]. This implies that liquid crystals have a long-range  
561 directional order, and the correlation length is limited by the cell thickness. Therefore the  
562 molecular dynamics can be modeled with boundary condition at the electrodes which gives a  
563 linear dependence of dielectric strength on the cell thickness [15,46,54,57]. Preliminary study  
564 of our materials shows that the dielectric strength of SPE relaxation process P1 is proportional  
565 to the thickness of the cell ( $d$ ) and the high permittivity in our systems can be attributed to the  
566 collective fluctuations of a very large number of molecules having the correlation length  $\sim d$   
567 like the other ferroelectric LCs mentioned above. However, there is big difference in the results  
568 obtained from dielectric spectroscopy of FLCs and our materials. The dielectric strength of  
569 ferroelectric materials is strongly dependent on bias voltage which suppresses the ferroelectric  
570 Goldstone response [13,15,54,57]. Contrary to this, the dielectric strength of our materials is  
571 practically independent of the bias voltage up to 35 V using Novocontrol Alpha Analyzer.  
572 Although the dielectric permittivity in N<sub>F</sub> and in our sample linearly depends on the cell  
573 thickness they have different physical origins, the phason mode in N<sub>F</sub> and the amplitude mode  
574 in SPE. This needs to be studied further.

575

#### 576 **4. Conclusion**

577 In this study, we have designed, synthesized, and investigated two novel compounds WJ-16  
578 and WJ-18, as modifications of the prototype DIO. The dipole moments determined using  
579 DFT are 10.4 and 14.8 D, respectively. Our original objective was the development of new  
580 ferroelectric nematic materials. Surprisingly, both materials show linear, non-ferroelectric,  
581 hysteresis-free P - E dependence. Recently Mandle [32] showed that the high magnitude of  
582 the dipole moment does not guarantee the formation of ferroelectric nematic phases.  
583 Madhusudana [29] theoretically showed the importance of the charge distribution along the  
584 molecule for the formation of ferroelectric state. Finally, Li *et al* [31] systematically analyzed  
585 more than 100 ferrogenic compounds and defined the Pearson's coefficient (or impact) of  
586 different parameters on the formation of the ferroelectric nematic phase. The most important  
587 parameters are magnitude of the dipole moment (0.26), the molecular length (0.19) and the

588 angle the dipole moment makes with the long molecular axis (0.16). The dipole moment itself  
589 the most important parameter, however it alone cannot guarantee the formation of the  
590 ferroelectric nematic phase. Both samples being non-ferroelectric show CP measured using  
591 dielectric spectrometer as well as using direct capacitance measurements of the LC cell with  
592 uncoated electrodes. Hence, the observed phenomenon is best described as superparaelectric  
593 rather than ferroelectric. This is the first direct demonstration of superparaelectricity in liquid  
594 crystalline organic materials. The results given in this manuscript highlight the anisotropic  
595 properties of the large dipole moment soft matter organic molecular system. The synergistic  
596 electrical properties are subtle, interesting, and potentially useful.

597

### 598 **Acknowledgment**

599 The work in Dublin was funded by the US-Ireland, SFI 21/US/3788. WJ thanks the CSC,  
600 China for a PhD scholarship. YT thanks Faculty of Engineering, University of Sheffield for  
601 his PhD studentship. MS thanks Prof. Manjuladevi V, BITS Pilani, India for allowing him to  
602 work as visiting student at Trinity College Dublin. The work in Sheffield was funded by  
603 EPSRC (EP-T003294). GHM thanks Diamond Light Source, UK for beamtime allocations  
604 SM31552 and SM33389. XZ thanks Dr. Olga Shebanova and Prof. Nick Terill at station I22,  
605 Diamond Light Source for help with SAXS/WAXS experiments.

606

### 607 **References**

- 
- [1] L. E. Cross, *Ferroelectrics*, 1987, **76**, 241-267]
  - [2] T. Park, Z. Nussinov, K. R. A. Hazzard, V.A. Sidorov, A.V. Balatsky, J.L. Sarrao, S.-W. Cheong, M.F. Hundley, Jang-Sik Lee, Q.X. Jia, and J.D. Thompson, *Phys. Rev. Lett.* 2005, **94**, 017002.
  - [3] X. Q. Liu, S. Y. Wu, X. M. Chen, H. Y. Zhu, *J. Appl. Phys.* 2008, **104**, 054114.
  - [4] N. N. Rabin, S. Ida, M. R. Karim, Md. S. Islam, R. Ohtani, M. Nakamura, M. Koinuma, L. F. Lindoy, S. Hayami, *ACS Omega* 2018, **3**, 2074–2083.
  - [5] K. Wang, J. Ouyang, M. Wuttig, Yu-Y. Zhao, H. Cheng, Y. Zhang, R. Su, J. Yan, X. Zhong, F. Zeng, *Adv. Energy Mater.* 2020, **10**, 2001778
  - [6] R. Waser, *Integrated Ferroelectrics*, 1997, **15**, 39-51.
  - [7] H. Nishikawa, K. Shiroshita, H. Higuchi, Y. Okumura, Y. Haseba, S. Yamamoto, K. Sago, H. Kikuchi. *Adv. Mater.* 2017, **29**, 1702354
  - [8] R. J. Mandle, S. J. Cowling, J. W. Goodby, *Phys. Chem. Chem. Phys.* 2017, **19**, 11429-35.

- 
- [9] X. Chen, E. Korblova, D. Dong, X. Wei, R. Shao, L. Radzihovsky, M. A. Glaser, J. E. Maclennan, D. Bedrov, D. M. Walba, N. A. Clark, *Proc. Natl. Acad. Sci. U.S.A.* 2020, **117**, 14021.
- [10] R. J. Mandle, S. J. Cowling, J. W. Goodby, *Liq. Cryst.* 2021, **48**, 1780.
- [11] N. Sebastian, M. Copic, A. Mertelj, *Phys. Rev. E*, 2022, **106**, 021011.
- [12] M. T. Máthé, B. Farkas, L. Péter, Á. Buka, A. Jákl, P. Salamon, *Scientific Reports* 2023, **13**, 6981.
- [13] N. Vaupotic et al. Dielectric response of a ferroelectric nematic liquid crystalline phase in thin cells. *Liquid Crystals* 2023, **50**, 584–595.
- [14] V. Matko, E. Gorecka, D. Pocięcha, J. Matraszek, N. Vaupotič. *Phys. Rev. Research* 2024, **6**, L042017
- [15] N. A. Clark, X. Chen, J.E. Maclennan, M.A. Glaser, *Phys. Rev. Research* 2024, **6**, 013195.
- [16] A. Erkoreka, J. Martinez-Perdiguero, R. J. Mandle, A. Mertelj, N. Sebastián, *J. Mol. Liquids*, 2023, 387, 122566.
- [17] A. Adaka, M. Rajabi, N. Haputhantrige, S. Sprunt, O. D. Lavrentovich, A. Jakli. *Phys. Rev. Lett.* 2024, **133**, 038101.
- [18] P. Kumari, B. Basnet, M. O. Lavrentovich, O. D. Lavrentovich, *Science* 2024, **383**, 1364–1368.
- [19] N. Yadav, Y. P. Panarin, W. Jiang, G. H. Mehl, J. K. Vij, *Phys. Chem. Chem. Phys.* 2023, **25**, 9083.
- [20] N. Yadav, Y. P. Panarin, J. K. Vij, W. Jiang, G. H. Mehl, *Liq. Cryst.* 2023, **50**, 1375–1382.
- [21] B. Basnet, M. Rajabi, H. Wang, P. Kumari, K. Thapa, S. Paul, M. O. Lavrentovich and O. D. Lavrentovich, *Nat. Comms*, 2022, **13**, 3932.
- [22] E. Cruickshank, *Chem. Plus. Chem.* 2024, **89**, e202300726.
- [23] H. Kikuchi, H. Matsukizono, K. Iwamatsu, S. Endo, S. Anan, Y. Okumura, *Adv. Sci.* 2022, **9**, 2202048.
- [24] Y. Song, J. Li, R. Xia, H. Xu, X. Zhang, H. Lei, W. Peng, S. Dai, S. Aya, M. Huang. *Phys. Chem. Chem. Phys.* 2022, **24**, 11536.
- [25] H. Matsukizono, K. Iwamatsu, S. Endo, Y. Okumura, S. Anan, H. Kikuchi, *J. Mater. Chem. C* 2023, **11**, 6183.
- [26] H. Nishikawa, F. Araoka, *Adv. Mater.* 2021, **33**, 2101305.
- [27] A. Manabe, M. Bremer, M. Kraska, *Liq. Cryst.* 2021, **48**, 1079.
- [28] A. A. Marchenko, O. L. Kapitanchuk, Y. Y. Lopatina, K. G. Nazarenko, A. I. Senenko, N. Katsonis, V. G. Nazarenko, O. D. Lavrentovich, *Phys Rev Lett* 2024, **132**, 098101.
- [29] N. V. Madhusudana, *Phys Rev. E* 2021, **104**, 014704.
- [30] O. E. Panarina, Yu. P. Panarin, F. Antonelli, J. K. Vij, M. Reihmann and G. Galli, *J. Mater. Chem.*, 2006, **16**, 842
- [31] J. Li, H. Nishikawa, J. Kougo, J. Zhou, S. Dai, W. Tang, X. Zhao, Y. Hisai, M. Huang, S. Aya, *Sci. Adv.* 2021, **7**, eabf5047.
- [32] J. Hobbs, C. J. Gibb, and R. J. Mandle, *Small Sci.* 2024, 2400189 .

- 
- [33] H. Nishikawa, K. Sano, S. Kurihara, A. Nihoyanagi, G. Watanabe, B. Dhara, F. Araoka *Commun. Mater.* 2022, **3**, 89.
- [34] X. Chen, E. Korblova, M. A. Glaser, J. E. Maclennan, D. M. Walba, N. A. Clark, *Proc. Natl. Acad. Sci.* 2021, **118**, e2104092118.
- [35] P. Rudquist, *Scientific Reports*, 2021, **11**, 24411.
- [36] I. Haller, *Prog. Solid State Chem.*, 1975, **10**, 103–118
- [37] C. B. Sawyer, C. H. Tower, *Phys. Rev. E*, 1939, **35**, 269.
- [38] H. Diamant, K. Drenck, R. Pepinsky, *Rev. Sci. Instrum.* 1957, **28**, 30.
- [39] C. Reynaerts, A. de Vos, *Ferroelectrics* 1991, **113**, 439.
- [40] Y. P. Panarin, *Mol. Mats.* 1993, **1**, 137 <https://doi.org/10.21427/1T6S-FZ03>
- [41] S. Kimura, S. Nishiyama, Y. Ouchi, H. Takezoe, A. Fukuda, *Japanese J. Appl. Phys.* 1987, **26**, L255.
- [42] V. M. Vaksman, Y.P. Panarin, *Mol. Mats.* 1992, **1**, 147 DOI: 10.21427/D7FF8R.
- [43] C. Filipic, T. Carlson, A. Levstik, B. Zekz, R. Blinc, F. Gouda, S. T. Lagerwall and K. Skarp, *Phys. Rev. A* 1988, **38**, 5833.
- [44] A. M. Biradar, S. S. Bawa, and Subhas Chandra, Dielectric relaxation in a high-tilt-angle chiral-nematic–smectic-C\* ferroelectric liquid crystal., *Phys.Rev.A*, **45**, 7282 (1992).
- [45] F. Gouda, W. Kuczynski, S. T. Lagerwall, M. Matuszczyk, T. Matuszczyk and K. Skarp, Determination of the dielectric biaxiality in a chiral smectic-C phase., *Phys.Rev.A*, **46**, 951 (1992).
- [46] Yu. P. Panarin, Yu. P. Kalmykov, S. T. Mac Lughadha, H. Xu and J. K. Vij, Dielectric Response of SSFLC Cells., *Phys.Rev.E*, **50**, 4763-4772 (1994).
- [47] M. Fukui, H. Orihara, A. Suzuki, Y. Ishibashi, Y. Yamada, N. Yamamoto, K. Mori, K. Nakamura, Y. Suzuki, I. Kawamura., Dielectric Dispersion in the Antiferroelectric Liquid Crystal MHPOBC., *Jpn.J.Appl.Phys.*, **29**, L329 (1990).
- [48] Yu. P. Panarin, O. E. Kalinovskaya and J. K. Vij, The investigation of the relaxation processes in AFLCs by broad band dielectric and electro-optic spectroscopy., *Liq.Cryst.*, **25(2)**, 241-252 (1998).
- [49] K. Hiraoka, A. Taguchi, Y. Liq.Cryst.,25(2),241-252u. Ouchi, H. Takezoe, A. Fukuda., *Jpn.J.Appl.Phys.*, **29**, L103 (1990).
- [50] Yu. P. Panarin, O. E. Kalinovskaya, J. K. Vij and J. W. Goodby., Observation and Investigation of the Ferrielectric Subphase with high qT parameter., *Phys.Rev.E*, **55**, 4345 (1997).
- [51] F. Kremer, S. U. Vallerien, R. Zentel, H. Kapitza, *Macromolecules*, 1989, **22**, 4040.
- [52] N. Yadav, Y. P. Panarin, J. K. Vij, W. Jiang, G. H. Mehl, *J. Mol. Liq.* 2023, **378**, 121570.
- [53] L. Guo, E. Gorecka, D. Pocięcha, N. Vaupotič, M. Čepič, R. A. Reddy, K. Gornik, F. Araoka, N. A. Clark, D. M. Walba, K. Ishikawa, H. Takezoe, *Phys. Rev. E* 2011, **84**, 031706.
- [54] S. Nakasugi, S. Kang, Tso-Fu. M. Chang, T. Manaka, H. Ishizaki, M. Sone, J. Watanabe, *J. Phys. Chem. B* 2023, **127**, 6585–6595.

- 
- [55] A. Erkoreka, A. Mertelj, M. Huang, S. Aya, N. Sebastian, and J. Martinez-Perdiguero, *J. Chem. Phys.* 2023, **159**, 184502.
- [56] S. Brown, E. Cruickshank, J. M. D. Storey, C. T. Imrie, D. Pocięcha, M. Majewska, A. Makal, E. Gorecka, *Chem. Phys. Chem.* 2021, **22**, 2506–2510.
- [57] M. Mrukiewicz, P. Perkowski, J. Karcz and P. Kula, *Phys. Chem. Chem. Phys.*, 25,13061 (2023).
- [58] M. Mrukiewicz, M. Czerwinski, N. Podoliak, D. Repcek, P. Perkowski, R. J. Mandle and D. Węłowska, Polar nematic phases with enantiotropic ferro- and antiferroelectric behaviour. *J. Mater. Chem. C* 2024, **12**, 7214–7224.
- [59] Ying-Hao Chu, Science Magazine - October 1 (2021).
- [60] H. Fröhlich, Theory of Dielectrics, Oxford University Press, 1958.
- [61] J. G. Kirkwood, *J. Chem. Phys.* 1939, **7**, 911.